Journal of The Electrochemical Society, **161** (6) A981-A988 (2014)
0013-4651/2014/161(6)/A981/8/$31.00 © The Electrochemical Society

Resolving Losses at the Negative Electrode in All-Vanadium Redox Flow Batteries Using Electrochemical Impedance Spectroscopy

Che-Nan Sun,[a,*,z] Frank M. Delnick,[b,*] Douglas S. Aaron,[c] Alexander B. Papandrew,[c,*] Matthew M. Mench,[a,d,*] and Thomas A. Zawodzinski Jr.[a,c,e,,z]**

[a]*Materials Science and Technology Division, Energy and Transportation Science Division, Oak Ridge National Laboratories, Oak Ridge, Tennessee 37831, USA*
[b]*Power Sources Technology Group, Sandia National Laboratories, Albuquerque, New Mexico 87185, USA*
[c]*Department of Chemical and Biomolecular Engineering, University of Tennessee, Knoxville, Tennessee 37996, USA*
[d]*Department of Mechanical, Aerospace, and Biomedical Engineering, University of Tennessee, Knoxville, Tennessee 37996, USA*
[e]*Department of Chemistry, King Abdulaziz University, Jeddah, Saudi Arabia*

We present an in situ electrochemical technique for the quantitative measurement and resolution of the ohmic, charge transfer and diffusion overvoltages at the negative electrode of an all-vanadium redox flow battery (VRFB) using electrochemical impedance spectroscopy (EIS). The mathematics describing the complex impedance of the V^{+2}/V^{+3} redox reaction is derived and matches the experimental data. The voltage losses contributed by each process have been resolved and quantified at various flow rates and electrode thicknesses as a function of current density during anodic and cathodic polarization. The diffusion overvoltage was affected strongly by flow rate while the charge transfer and ohmic losses were invariant. On the other hand, adopting a thicker electrode significantly changed both the charge transfer and diffusion losses due to increased surface area. Furthermore, the Tafel plot obtained from the impedance resolved charge transfer overvoltage yielded the geometric exchange current density, anodic and cathodic Tafel slopes (135 ± 5 and 121 ± 5 mV/decade respectively) and corresponding transfer coefficients $\alpha = 0.45 \pm 0.02$ and $\beta = 0.50 \pm 0.02$ in an operating cell.

Manuscript submitted January 16, 2014; revised manuscript received March 25, 2014. Published April 30, 2014.

Consumption of fossil energy can be reduced by enhancing the utilization of renewable energy sources. However, the intermittent and often unpredictable nature of renewable energy, such as wind and solar, pose a challenge to widespread implementation.[1] To effectively integrate the energy from more diverse resources to the modern grid, large-scale energy storage systems are required as mediators through load leveling and peak shaving.[2] Redox flow batteries (RFBs) are an energy storage system that meets many of the requirements for this application.[3,4]

Unlike conventional batteries, RFBs are able to decouple power and energy capacities. During RFB operation, the negative and positive reactants are circulated to the battery stack for electrochemical reaction from separated reservoirs. In a RFB, the available power is determined by the characteristics of the battery stack while energy is controlled by the electrolyte properties and the size of electrolyte reservoirs. Nevertheless, to be economically viable, a critical factor is RFB capital cost.

Among RFBs, the vanadium redox flow battery (VRFB)[5–9] has attracted the most attention in recent years.[10–17] The installed cost of the VRFB is strongly associated with the energy density (electrolyte concentration) and the power density (stack performance) of the system.[18] Kazacos et al.[19] and, more recently, researchers at Pacific Northwest National Laboratory (PNNL)[20] have reported advanced electrolytes with higher energy density. On the other hand, the stack performance was substantially enhanced by the research group at the University of Tennessee-Knoxville (UTK) using a "zero-gap" cell design.[21,22] These critical achievements have made the VRFB a promising technology for grid-scale energy storage application.

To further improve battery performance, one must identify and quantify the rate-limiting processes that control the losses in the cell. In previous work, we demonstrated that the voltage losses originating from charge transfer and ohmic processes at various discharge currents can be quantified using electrochemical impedance spectroscopy (EIS); and these losses were dominant at the negative electrode.[23] However, we were not able to quantify diffusion overvoltage at that time.

In this work, we again apply EIS to probe the voltage losses at the VRFB negative electrode. We present a complex impedance protocol which allows quantitative measurement and resolution of the overvoltages resulting from ohmic, charge transfer and diffusion processes at various operating current densities during charge and discharge. We demonstrate this protocol by measuring these overvoltages as a function of flow rate and electrode thickness. The results clearly identify and quantify the rate limiting processes at various charge/discharge currents and cell configurations leading to a pathway for performance optimization.

Experimental

Electrolyte system.— Vanadium electrolyte solutions containing 0.8M total vanadium ions and 4M sulfuric acid were prepared using a protocol described previously.[23] In particular, the negative half-cell (V^{2+}/V^{3+}) was the focus of this work and was tuned close to 50% state of charge (SoC) with a volume of 400 mL. The flow rate was maintained by either a gravity siphon (1.5 mL/min) or a peristaltic pump (8 mL/min and 40 mL/min).

Cell.— A 5 cm^2 single cell (Fuel Cell Technologies) with PTFE-coated fiberglass cell gaskets was adopted in this work. Carbon paper (SGL 10AA, 400 microns thick, <12 mΩ-cm) was used as the electrode material for both sides of the cell. The thickness of the gasket was chosen to achieve 25% compression of the electrodes upon cell closure. Two pieces of Nafion 117 (Ion Power) were used as the separator. A dynamic hydrogen electrode[24,25] and a $Hg/HgSO_4$ electrode were used as reference electrodes in this work. In the latter case, the tip of the $Hg/HgSO_4$ electrode was placed on the Nafion membrane at the perimeter of the cell and the junction point was wetted with 0.5 M H_2SO_4.

Impedance measurement.— Electrochemical impedance spectroscopy (EIS) was performed in a symmetric cell. The negative electrolyte was purged with ultra-high-purity nitrogen gas and circulated to both sides of the cell from a single reservoir. We set the initial $[V^{+2}]/[V^{+3}]$ ratio to correspond to a SoC of 50%. With this configuration, a change in the $[V^{+2}]/[V^{+3}]$ ratio at the working electrode during charge/discharge was precisely compensated by an opposite change in the ratio at the counter electrode.[26] This cell configuration also

*Electrochemical Society Active Member.
**Electrochemical Society Fellow.
zE-mail: chenan.sun@gmail.com; tzawodzi@utk.edu

eliminated self-discharge caused by oxygen oxidation of the V^{+2} and by vanadium ion crossover through the membrane. This cell does not, however, eliminate concentration variations caused by self discharge (V^{+2} oxidation) against the H^+ reduction reaction within the cell stack.[27] This side reaction is particularly important when conducting long term complex impedance measurements to very low frequencies. Under these circumstances the $[V^{+2}]/[V^{+3}]$ ratio can be reduced by almost 2 orders of magnitude. When this happened the $[V^{+2}]/[V^{+3}]$ ratio was estimated using the Nernst equation at the open circuit potential measured with respect to the reference electrode. Charge and discharge of the V^{+2}/V^{+3} anode were performed potentiostatically by polarizing the working electrode with respect to the reference electrode potential. The impedance of the working electrode was measured using a 5 mV sinusoidal perturbation superimposed onto the DC polarization potential, as described previously.[23] The cell, the pump and the electrolyte reservoir were maintained in a temperature chamber (Yamato) at 30°C.

Results and Discussion

Mathematical model.— We previously investigated the voltage loss of a VRFB using the EIS technique combined with a reference electrode and observed that the total overvoltage within the cell was dominated by the negative electrode.[23] In this report we examine in greater detail the individual rate-limiting processes which contribute to this total overvoltage at the anode. In order to describe the complex impedance of the V^{+2}/V^{+3} redox reaction, we use the theory of electrochemical impedance of macrohomogeneous porous electrodes derived by Paasch, Micka and Gersdorf[28] and expressed in general form by equations 1 and 2.

$$AZ_p = \frac{\left(\rho_1^2+\rho_2^2\right)b}{(\rho_1+\rho_2)}\frac{\coth Q_2}{Q_2} + \frac{2\rho_1\rho_2 b}{(\rho_1+\rho_2)\,Q_2\sinh Q_2} + \frac{\rho_1\rho_2 b}{(\rho_1+\rho_2)} \quad [1]$$

$$Q_2 = \sqrt{\frac{(\rho_1+\rho_2)\,bA_t}{AZ_a}} \quad [2]$$

The symbols used throughout this report are defined in Appendix I.

In equation 1, Z_p is the complex impedance of the porous electrode. In equation 2, Z_a is the complex impedance of a differential unit element of surface area within the electrode. Z_a represents the impedance of the charge transfer reaction, Z'_a, connected in parallel with the double layer capacitance (shown as a constant phase element) in equation 3.

$$\frac{1}{Z_a} = \frac{1}{Z'_a} + (j\omega)^P C_{dl} \quad [3]$$

The general form of the charge transfer impedance, Z'_a, can be derived from the Butler-Volmer equation for the specific charge transfer reaction. For the VRFB, the charge transfer reaction at the negative electrode is given by equation 4.

$$V^{+3} + e^- \langle = \rangle V^{+2} \quad [4]$$

The corresponding Butler-Volmer relation is shown in equation 5.

$$i = i_o\left\{\frac{[V^{+2}]_o}{[V^{+2}]_b}\exp\left(\alpha\frac{F}{RT}\eta\right) - \frac{[V^{+3}]_o}{[V^{+3}]_b}\exp\left(-\beta\frac{F}{RT}\eta\right)\right\} \quad [5]$$

And the resulting charge transfer impedance, Z'_a, is shown in equation 6.

$$Z'_a = \frac{RT}{i_o F G_\eta} - \frac{RTM_\eta}{F[V^{+2}]_b G_\eta}\frac{d[V^{+2}]_{os}}{di_s} + \frac{RTN_\eta}{F[V^{+3}]_b G_\eta}\frac{d[V^{+3}]_{os}}{di_s} \quad [6]$$

where

$$M_\eta = \exp\left(\alpha\frac{F}{RT}\eta_s\right) \quad [7]$$

$$N_\eta = \exp\left(-\beta\frac{F}{RT}\eta_s\right) \quad [8]$$

$$G_\eta = \alpha\frac{[V^{+2}]_{os}}{[V^{+2}]_b}M_\eta + \beta\frac{[V^{+3}]_{os}}{[V^{+3}]_b}N_\eta \quad [9]$$

In equations 6 – 9 the subscript, s, refers to the Laplace transform variable $s = \sigma + j\omega$. And i_s, η_s, $[V^{+2}]_{os}$ and $[V^{+3}]_{os}$ are the Laplace transforms of the current, overvoltage and surface concentrations respectively.

The steady-state area specific impedance, Z'_a, is obtained after the derivatives $\frac{d[V^{+2}]_{os}}{di_s}$ and $\frac{d[V^{+3}]_{os}}{di_s}$ are evaluated from the appropriate Laplace transformed diffusion equations (see discussion below), and the neperian frequency, σ is suppressed (σ→0) so that $s \rightarrow j\omega$.

The Paasch model does not assign any specific geometry to the electrode pore structure or surface area elements within the pore structure. Instead, the influence of geometric shape and form are included at a microscopic scale in the definition of Z'_a. Specifically, the solution of Fick's first and second laws of diffusion, which is required for evaluation of the derivatives $\frac{d[V^{+2}]_{os}}{di_s}$ and $\frac{d[V^{+3}]_{os}}{di_s}$, is typically conducted in a geometric framework which establishes the boundary conditions for the mathematical solution. At this time, however, we will continue to ignore geometric shape and form and only utilize one-dimensional solutions to the diffusion equations. Later, we will address geometric shape and form as a correction to the one-dimensional solutions.

When the porous negative electrode of a vanadium redox flow battery is discharged without flowing electrolyte, the $[V^{+2}]$ concentration in the pore structure is quickly depleted and the discharge is limited by diffusion to the back surface of the electrode at the flow channels. When electrolyte is flowing, however, a Nernstian diffusion layer is established at the back surface and within the pore structure of the electrode. The thickness of the Nernstian diffusion layer, a, is governed by the hydrodynamics of the electrolyte flow; and the concentrations of the oxidized and reduced species are maintained constant at the boundary of the Nernstian diffusion layer. Jacobsen and West[29] derived the one-dimensional Laplace transformed diffusion equation for a uniform Nernstian finite diffusion layer from which we computed the concentration derivatives required in equation 6:

$$\frac{d[V^{+2}]_{os}}{di_s} = -\frac{\tanh\left(a\sqrt{\frac{s}{D_R}}\right)}{F\sqrt{sD_R}} \quad [10]$$

$$\frac{d[V^{+3}]_{os}}{di_s} = \frac{\tanh a\sqrt{\frac{s}{D_O}}}{F\sqrt{sD_O}} \quad [11]$$

Substitution of equations 10 and 11 into equation 6 yields equation 12 when s→ jω.

$$Z'_{a1} = \frac{RT}{Fi_oG_\eta} + \frac{RTM_\eta a}{F^2[V^{+2}]_bD_RG_\eta}\frac{\tanh\left(a\sqrt{\frac{j\omega}{D_R}}\right)}{a\sqrt{\frac{j\omega}{D_R}}} + \frac{RTN_\eta a}{F^2[V^{+3}]_bD_OG_\eta} \times \frac{\tanh\left(a\sqrt{\frac{j\omega}{D_O}}\right)}{a\sqrt{\frac{j\omega}{D_O}}} \quad [12]$$

Equation 12 describes the impedance of the charge transfer reaction at each differential unit element of surface area within the porous electrode when the finite diffusion layer is constant throughout the electrode. This is clearly not the case when electrolyte is flowing across the back surface of the electrode. Electrolyte shear varies with electrode depth and pore size. We therefore expect a distribution in the Nernstian diffusion layer thickness, a. Nevertheless, commensurate with our use of the one-dimensional model, we consider the parameter, a, in equation 12 as an "average" diffusion layer thickness.

We also expect that a significant fraction of the internal surface resides in pores which support little or no electrolyte flow, and for

which the pore size is much smaller than the Nernstian diffusion layer. For these surface area elements equations 12 does not apply.

Instead, finite diffusion is limited by the size of the pores (p = pore size) and the analogous charge transfer impedance at these unit differential elements of surface area is given by equation 13.

$$Z'_{a2} = \frac{RT}{Fi_oG_\eta} + \frac{RTM_\eta \frac{p}{2}}{F^2[V^{+2}]_bD_RG_\eta}\frac{\coth\left(\frac{p}{2}\sqrt{\frac{j\omega}{D_R}}\right)}{\frac{p}{2}\sqrt{\frac{j\omega}{D_R}}} + \frac{RTN_\eta \frac{p}{2}}{F^2[V^{+3}]_bD_OG_\eta}\frac{\coth\left(\frac{p}{2}\sqrt{\frac{j\omega}{D_O}}\right)}{\frac{p}{2}\sqrt{\frac{j\omega}{D_O}}} \quad [13]$$

We recognize that the pore size is neither constant nor uniform within the electrode. The parameter, p, depends on pore geometry and is also distributed. Nevertheless, consistent with our treatment of the parameter, a, in equation 12, we also consider the parameter, p, in equation 13 as an "average" pore size.

By this simplified discussion, we show that the complex impedance of a differential element of surface within the porous anode depends very much on the boundary conditions that are assumed in the solution of the diffusion equations, and these boundary conditions vary with the hydrodynamic flow pattern within the electrode. We recognize that the overall impedance of the electrode will derive from a complex combination of Z'_{a1} elements and Z'_{a2} elements. We do not intend to establish this complex relationship. Nor do we intend to devise the distributions in the parameters "a" and "p" and their relationship to electrolyte hydrodynamics and pore geometry. Instead, we intend to quantify the voltage losses associated with migration, charge transfer reaction and diffusion processes. For this purpose, we do not need in-depth understanding of the complex impedance for these processes, we only need to know the current-dependent resistances associated with these processes. These ohmic, charge transfer, and diffusion resistances are derived by extrapolation of the corresponding complex impedances to the resistance axis of the Nyquist plot. And, these extrapolations can be made by using low frequency approximations to the corresponding impedance equations. In the following discussion, it is important to recognize that the parameters that define "low frequency" for the migration of ions within a porous electrode are different than the parameters that define "low frequency" for charge transfer reaction or for finite diffusion of vanadium ions. Therefore, the complex impedance of a porous electrode can have several low frequency intercepts at several different resistances. The overall purpose of this discussion is to associate each low frequency intercept and its corresponding resistance with a specific electrochemical or physical process and then integrate that resistance with respect to the steady-state polarization current to obtain a quantitative measure of the voltage loss (overvoltage) attributed to that specific process. Therefore:

In consideration of equations 1 and 2, in the limit as $\omega \to 0$, then $Z_a \to Z'_a$, and if

$$\frac{Z_a}{A_t} \gg \frac{(\rho_1+\rho_2)b}{A} \quad \text{then} \quad Q_2 \to 0 \quad [14]$$

And we can use the low frequency approximations:

$$\frac{coth\,Q_2}{Q_2} \to \frac{1}{3} + \frac{1}{Q_2^2} \quad \text{and} \quad Q_2 \sinh Q_2 \to Q_2^2 \quad [15]$$

Under these circumstances equation 1 reduces to equation 16.

$$AZ_p = \frac{b(\rho_1+\rho_2)}{3} + \frac{b\rho_1\rho_2}{3(\rho_1+\rho_2)} + \frac{AZ_a}{A_t} \quad [16]$$

Equation 16 is the low frequency approximation of equation 1.
In equation 16:

$$R_{hf} = \text{Ohmic Resistance} = \frac{b(\rho_1+\rho_2)}{3} + \frac{b\rho_1\rho_2}{3(\rho_1+\rho_2)} \quad [17]$$

In consideration of equation 12 in the limit as $\omega \to 0$:

$$\omega \ll \frac{D_R}{a^2} \quad \text{and} \quad \omega \ll \frac{D_O}{a^2}, \quad \text{then} \quad \frac{tanh\left(a\sqrt{\frac{j\omega}{D_R}}\right)}{a\sqrt{\frac{j\omega}{D_R}}} \to 1 \quad \text{and} \quad \frac{tanh\left(a\sqrt{\frac{j\omega}{D_O}}\right)}{a\sqrt{\frac{j\omega}{D_O}}} \to 1 \quad [18]$$

Equation 12 reduces to equation 19.

$$Z'_{a1} = \frac{RT}{Fi_oG_\eta} + \frac{RTM_\eta a}{F^2[V^{+2}]_bD_RG_\eta} + \frac{RTN_\eta a}{F^2[V^{+3}]_bD_OG_\eta} \quad [19]$$

Equation 19 is the low frequency approximation of equation 12.
In consideration of equation 13 in the limit as $\omega \to 0$:

$$\omega \ll \frac{4D_R}{p^2} \quad \text{and} \quad \omega \ll \frac{4D_O}{p^2} \quad [20]$$

$$\frac{\coth\left(\frac{p}{2}\sqrt{\frac{j\omega}{D_R}}\right)}{\left(\frac{p}{2}\sqrt{\frac{j\omega}{D_R}}\right)} \to \frac{1}{3} - j\frac{4D_R}{\omega p^2} \quad \text{and} \quad \frac{\coth\left(\frac{p}{2}\sqrt{\frac{j\omega}{D_O}}\right)}{\left(\frac{p}{2}\sqrt{\frac{j\omega}{D_O}}\right)} \to \frac{1}{3} - j\frac{4D_O}{\omega p^2} \quad [21]$$

Equation 13 reduces to equation 22.

$$Z'_{a2} = \frac{RT}{Fi_0G_\eta} + \frac{RTM_\eta}{F^2[V^{+2}]_bD_RG_\eta}\left(\frac{p}{6} - j\frac{2D_R}{p\omega}\right) + \frac{RTN_\eta}{F^2[V^{+3}]_bD_OG_\eta}\left(\frac{p}{6} - j\frac{2D_O}{p\omega}\right) \quad [22]$$

Equation 22 is the low frequency approximation of equation 13.
Equations 19 and 22 are further simplified with the following definitions:

$$R_{ct} = \frac{RT}{Fi_0G_\eta} = \text{charge transfer resistance} \quad [23]$$

$$W = \left(\frac{RTM_\eta}{F^2[V^{+2}]_bD_RG_\eta} + \frac{RTN_\eta}{F^2[V^{+3}]_bD_OG_\eta}\right) \quad [24]$$

Equation 19 reduces to equation 25:

$$Z'_{a1} = R_{ct} + aW \quad [25]$$

Equation 25 is the low frequency approximation to equation 12.
And equation 22 reduces to equation 26:

$$Z'_{a2} = R_{ct} + \frac{p}{6}W - j\frac{1}{\omega C_{fd2}} \quad [26]$$

Equation 26 is the low frequency approximation to equation 13.
In equation 26:

$$\frac{1}{C_{fd2}} = \frac{2}{p}\frac{RT}{F^2G_\eta}\left(\frac{M_\eta}{[V^{+2}]_b} + \frac{N_\eta}{[V^{+3}]_b}\right) \quad [27]$$

By comparing equations 25 and 26 we notice a very important difference in the low frequency impedance behavior of surface area elements, Z'_{a1}, which are controlled by finite diffusion to a Nernstian layer (non-blocking boundary condition) compared to area elements, Z'_{a2}, which are controlled by finite diffusion within the walls of the pores (blocking boundary condition). Specifically, at low frequency, Z'_{a1} is represented as a charge transfer resistance, R_{ct}, in series with a finite diffusion resistance, $R_{fd1} = aW$. On the other hand, Z'_{a2}, is represented by the same charge transfer resistance in series with a finite diffusion resistance, $R_{fd2} = \frac{p}{6}W$, and finite diffusion capacitance, C_{fd2}. We specifically note that the finite diffusion resistances for each surface area element only differ by the scale factors that are proportional to the average Nernstian diffusion layer thickness and average pore size respectively.

This simple model relies on one-dimensional solutions to Fick's first and second laws of diffusion for non-blocking (Nernstian) and blocking boundary conditions. We have not considered geometric shape and form and the distribution of these geometric parameters in the definition of the complex impedance of differential surface elements within the porous electrode.

When specific geometric shape and form are considered for differential surface elements and to describe the boundary conditions for finite diffusion to these elements[29,30] then a variety of different shapes yield complex impedance similar to equation 25 for non-blocking boundary conditions and similar to equation 26 for blocking conditions when extrapolated to low frequency. Except that the finite diffusion resistances and finite diffusion capacitances are scaled by different geometric parameters. For both boundary conditions, the charge transfer resistance does not depend on geometric shape and form and it only scales inversely with the total surface area. Therefore, we define the effective impedance of a differential element of surface by equation 28.

$$Z'_a = \frac{RT}{Fi_oG_\eta} + \frac{RTM_\eta a}{fF^2[V^{+2}]_b D_R G_\eta} \frac{\tanh\left(a\sqrt{\frac{j\omega}{D_R}}\right)}{a\sqrt{\frac{j\omega}{D_R}}} + \frac{RTN_\eta a}{fF^2[V^{+3}]_b D_O G_\eta} \frac{\tanh\left(a\sqrt{\frac{j\omega}{D_O}}\right)}{a\sqrt{\frac{j\omega}{D_O}}} \quad [28]$$

With corresponding low frequency approximation shown in equation 29.

$$Z'_a = R_{ct} + \frac{a}{f}W \quad [29]$$

Equation 28 is identical to equation 12 except that we have included the scale factor, *f*, in the denominator of the finite diffusion terms to account for geometric shape and form and their distributions within the electrode. We also note that at low frequencies (defined by equation 20), the impedance of Z'_{a2} elements contribute negligibly to the total impedance when added in parallel with the Z'_{a1} elements. In other words, only that fraction of the electrode surface which is controlled by finite diffusion to a Nernstian layer contributes to the finite diffusion resistance of the electrode. In this sense, the factor, *f*, also accounts for the partitioning of the total surface area into Z'_{a1} and Z'_{a2} elements. Strictly speaking, this rational for accommodating the complex distribution of the parameters *a* and *p*, and the effects of geometric shape and form, into a single scale factor is only justified at low frequency. Nevertheless, we have incorporated the factor,*f*, in the generalized impedance equation 28 and apply it over the entire frequency range of the complex impedance measurement.

In order to model the VRFB anode, we numerically solve equations 1, 2, 3 and 28 simultaneously using "*a*" and "*f*" as adjustable parameters to obtain the ohmic resistance, R_{hf}, (equation 17), the charge transfer resistance, R_{ct} (equation 29), and the finite diffusion resistance, $\frac{a}{f}W$, (equation 29) at the appropriate intercepts on the resistance axis of the Nyquist plots of the complex impedance of the VRFB anode.

Experimental results.— Figure 1A shows the measured Nyquist impedance spectra at open circuit for a single-layer V^{+2}/V^{+3} anode in a symmetric redox flow cell at 30°C. In order to make stable complex impedance measurements to low frequency (1 mHz) a gravity siphon was used to control the electrolyte flow rate at 1.5 mL/min. (When a peristaltic pump is used, the flow pulse created by the pump, causes a low frequency fluctuation (disturbance) in the diffusion layer which compromises the impedance measurement at low frequency.) Figure 1A also shows the complex impedance spectra computed using equations 1, 2 and 3 when Z'_a is defined by equation 28. The measured and computed resistance and reactance are also plotted as a function of frequency in Figure 1B. The parameters that were used to obtain this fit are shown in Appendix II. The close agreement between the measured impedance and the model allow us to extrapolate the ohmic resistance at the high frequency intercept, and the charge transfer resistance and finite diffusion resistance from the appropriate low frequency intercepts described above.

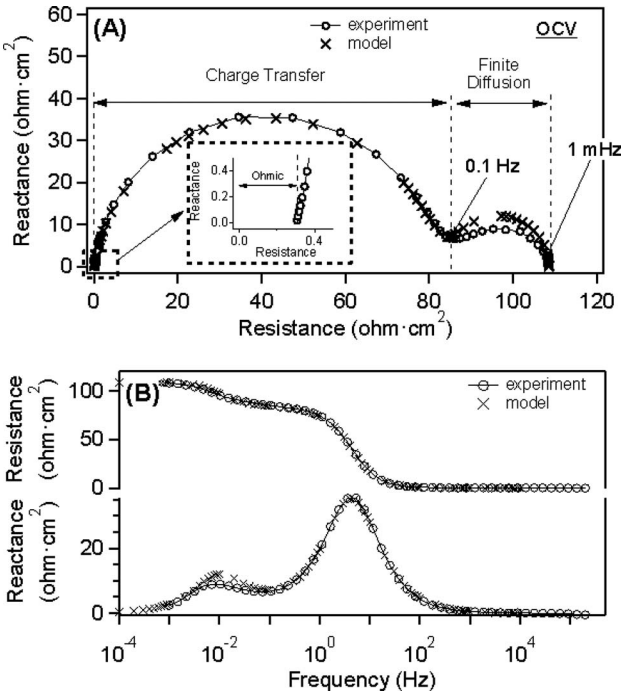

Figure 1. (A) Measured complex impedance spectrum of a V^{+2}/V^{+3} single-layer anode, at 30°C and flow rate of 1.5 mL/min, and complex impedance spectrum computed using equations 1, 2, 3 and 28. (B) Frequency dispersion of the resistance and reactance components of the impedance vectors in (A). Parameters used for the mathematical fit are shown in Appendix II.

The intercept at high frequency is the resistance of all ohmic processes in the cell. This includes the electronic and ionic resistance within the electrode (defined in equation 17) and the resistance resulting from charge migration through the Nafion membrane separator. The semicircle at frequencies above 0.1 Hz defines the impedance of the charge transfer process at the electrode surface which can be represented by a charge transfer resistance in parallel with a double-layer capacitance (represented as a constant phase element).[23] The impedance between 0.1 Hz to 1 mHz is defined by the Nernstian finite diffusion process within the porous electrode and permits the measurement of a finite diffusion resistance at the low frequency intercept with the resistance axis.

Selected complex impedance spectra at various anodic polarizations versus the reference electrode are shown in Figure 2. The ohmic

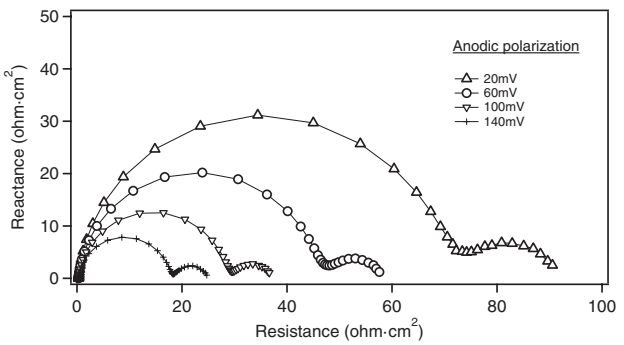

Figure 2. Selected electrochemical impedance spectra at 20 mV, 60 mV 100 mV and 140 mV anodic polarizations. Measurements were conducted at 30°C and flow rate of 1.5 mL/min on a single layer electrode.

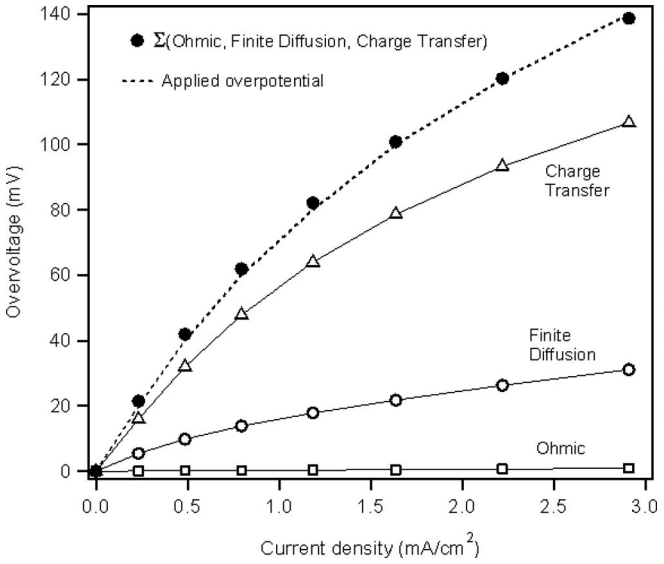

Figure 3. Overvoltages associated with the ohmic, charge transfer and finite diffusion processes in the V^{+2}/V^{+3} electrode under anodic polarization at 30°C and flow rate of 1.5 mL/min. Each overvoltage is obtained by integration (with respect to current density) of the corresponding ohmic resistance, charge transfer resistance and finite diffusion resistance defined in Figure 1A. Note: the sum of the ohmic + charge transfer + finite diffusion overvoltages is equal to the total applied overvoltage (dashed line).

resistance, charge transfer resistance and finite diffusion resistance are easily resolved from each spectrum respectively. The corresponding overvoltage associated with each resistance is then obtained by integrating each resistance with respect to the measured steady state current density as shown in Figure 3. The summation of the component overvoltages obtained from the integration of these resistances matches perfectly with the total measured overvoltage also shown in Figure 3. This plot confirms that the impedance spectra completely define and resolve all of the rate-limiting processes in the cell and that no other processes contribute to the voltage loss in the cell. However, complex impedance measurements to low frequency are very time consuming, and the long duration of the experiments result in a substantial decrease in the $[V^{+2}]/[V^{+3}]$ ratio (as described in the experimental section), and a corresponding change in the charge transfer resistance and finite diffusion resistance.

Therefore, in order to avoid time consuming impedance measurements to very low frequencies, we hereafter establish the diffusion overvoltage by measuring the total applied overvoltage and subtracting the impedance resolved ohmic overvoltage and impedance resolved charge transfer overvoltage. This process takes about four minutes and does not result in a change in the $[V^{+2}]/[V^{+3}]$ ratio. This procedure also allows us to use a peristaltic pump and perform experiments a higher electrolyte flow rates.

The charge transfer overvoltage with associated double layer capacitance, ohmic overvoltage and finite diffusion overvoltage for a single layer electrode (400 μm) at two different flow rates (8 mL/min and 40 mL/min) are shown in Figure 4. The working electrode was polarized both cathodically and anodically showing the behavior of a VRFB anode during charge and discharge, respectively.

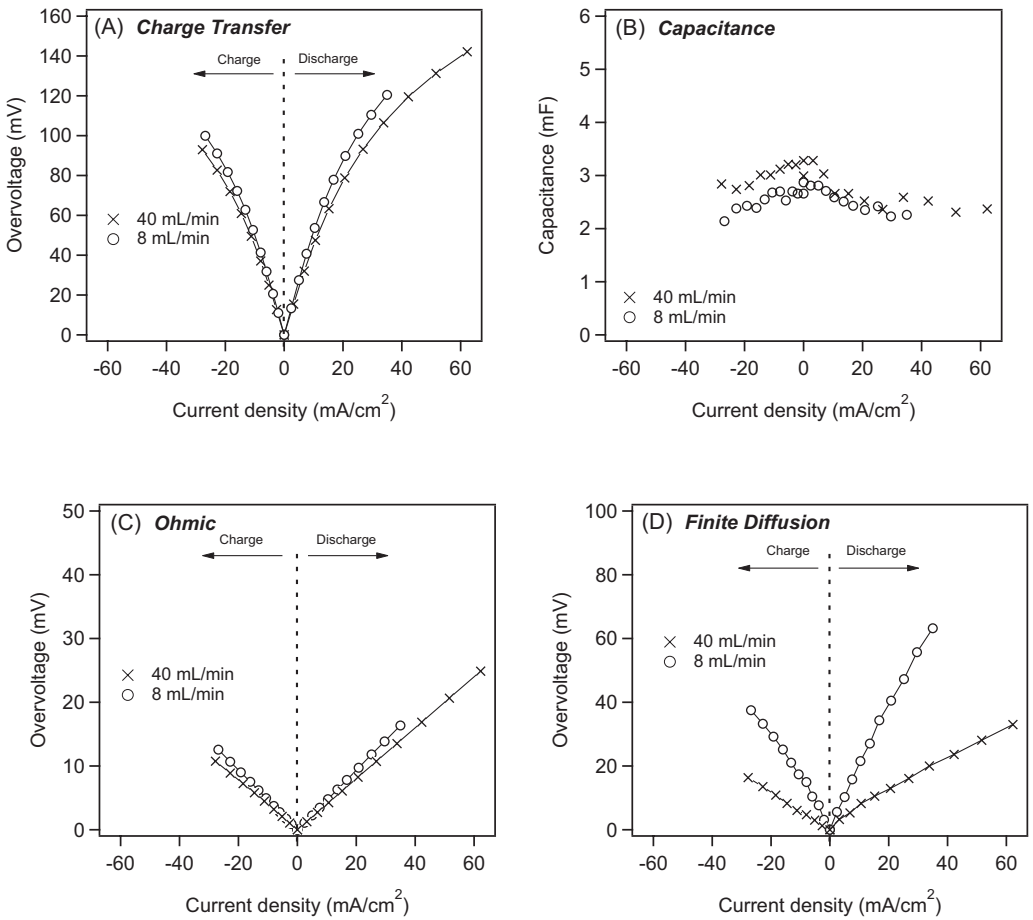

Figure 4. (A) charge transfer overvoltage (B) double-layer capacitance (C) ohmic overvoltage and (D) finite diffusion overvoltage in a single-layer electrode as a function of current density.

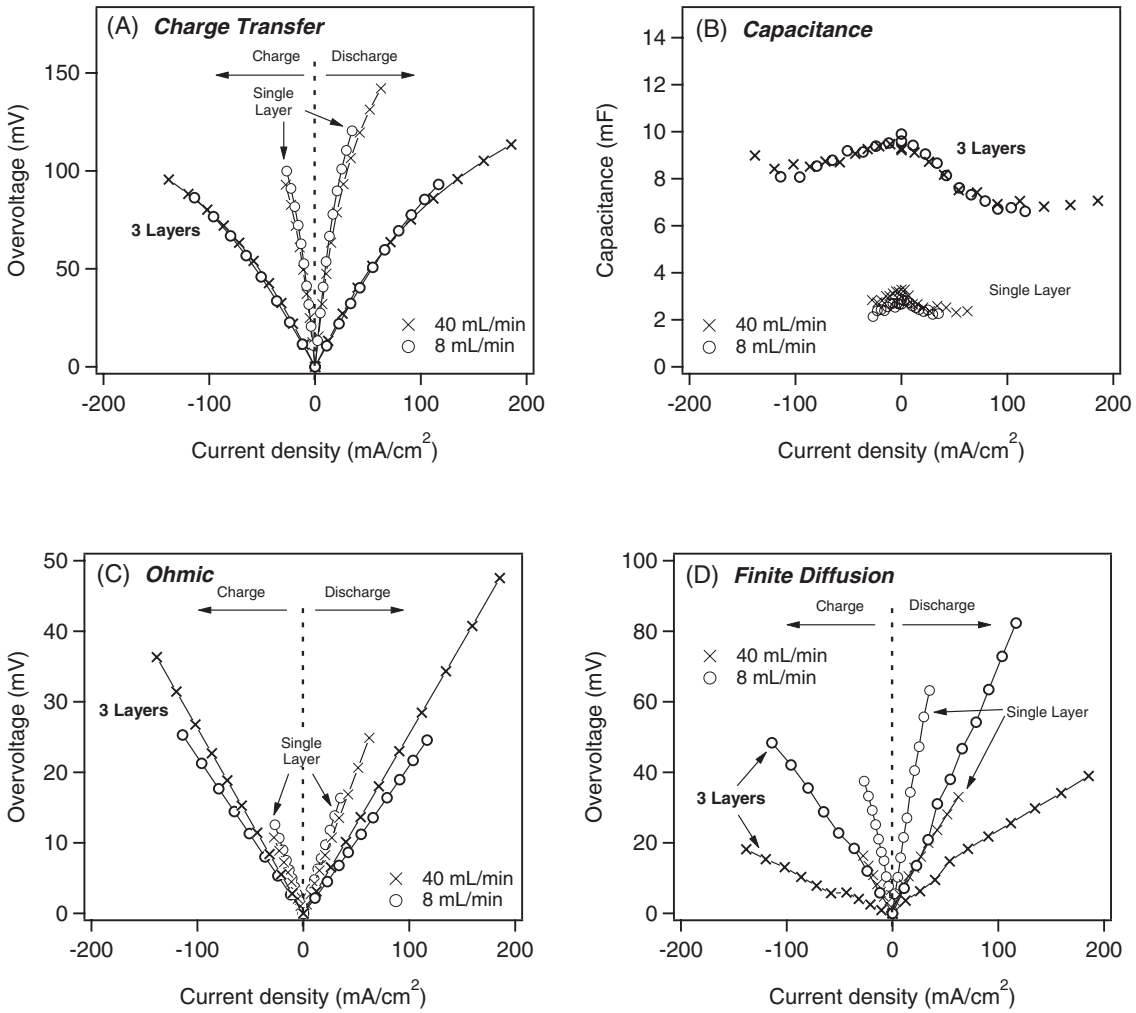

Figure 5. (A) charge transfer overvoltage (B) double-layer capacitance (C) ohmic overvoltage and (D) finite diffusion overvoltage in a 3-layers electrode electrode as a function of current density. Data for a single layer electrode are included for comparison.

It is clearly shown in Figure 4 that the charge transfer (Figure 4A) and ohmic overvoltages (Figure 4C) are invariant as flow rate changes; whereas the diffusion overvoltage (Figure 4D) is significantly reduced as flow rate increases. The double-layer capacitance shown in Figure 4B suggests that the surface area for the charge transfer was not strongly affected by the flow rate. In addition, the charge transfer processes contributes the largest portion of the total voltage loss within this current range.

Figure 5 shows results obtained under identical testing conditions as Figure 4, except the electrodes were stacked with 3 layers of 10AA (1200 μm total thickness).The maximum current density during charge and discharge was more than double compared to the single-layer electrode setup, indicating the overall performance was significantly enhanced. The double-layer capacitance (Figure 5B) increased by a factor of 3 compared to that for single-layer electrode suggesting the electrochemical surface area scaled proportionally with the electrode thickness. Figure 5A shows the charge transfer overvoltage was significantly reduced due to the increased surface area and was unaffected by flow rate. Figure 5D shows the diffusion overvoltage was also reduced significantly with the increased surface area and, as expected, was affected by the flow rate. Figure 5C shows a decrease in ohmic overvoltage for the three-layer electrode. This is counterintuitive. We surmise (without further evidence) that the membrane and electrodes were reduced in thickness by higher compression in this cell configuration leading to the reduced resistance. Overall, the charge transfer process still exhibits the largest contribution to the overall voltage loss.

A Tafel plot can be constructed using the impedance-resolved charge transfer overvoltage as shown in Figure 6. For a single elec-

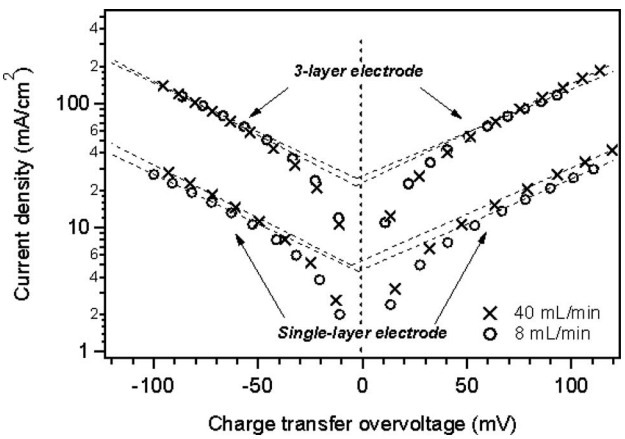

Figure 6. Tafel plots of the impedance resolved charge transfer overvoltages for single-layer and 3-layer electrodes at 30°C and flow rates of 8 mL/min and 40 mL/min.

Table I. Summary of the kinetic parameters including geometric exchange current density i_o, Tafel slopes and corresponding transfer coefficients extracted from Figure 6.

Electrode thickness (μm)	400				1200			
Flow rate (ml/min)	8		40		8		40	
Geometric i_o (mA/cm^2)	4.4		5.0		25.0		21.8	
	charge	discharge	charge	discharge	charge	discharge	charge	discharge
Tafel slope (mV/decade)	125.4	136.7	117.0	134.6	126.3	143.3	114.7	125.4
Transfer coefficient	0.48	0.44	0.51	0.45	0.48	0.42	0.52	0.48

tron, outersphere electron transfer we expect symmetric redox kinetics and we expect the transfer coefficients to be independent of electrolyte flow rate and electrode thickness. In Table I, we report 4 measurements for each coefficient with $\alpha = 0.45 \pm 0.02$ and $\beta = 0.50 \pm 0.02$. Previous studies have reported $\alpha = 0.29$, $\beta = 0.30$;[25] and $\alpha = 0.31$, $\beta = 0.26$[31] respectively. By comparison with this earlier work, our impedance resolved measurements of these transfer coefficients appears more appropriate and representative of the electrode kinetics.

Conclusions

We have demonstrated a technique to quantify the in-situ ohmic, charge transfer and diffusion overvoltages at the negative electrode of the all-vanadium redox flow battery during charge and discharge. Voltage loss from each process was probed as the electrode thickness (400 μm and 1200 μm) and flow rate (8 mL/min and 40 mL/min) varied. Charge transfer and diffusion overvoltage both decreased as the electrode thickness increased implying electrode surface area is a crucial factor affecting the battery performance. However, only the diffusion overvoltage decreased as the flow rate was increased. Tafel plots constructed using impedance resolved charge transfer overvoltage allowed us to investigate in-situ kinetics in more detail. Tafel slopes and corresponding charge transfer coefficients were observed close to ideal values expected for a one-step one-electron process at the negative electrode of the all-vanadium redox flow battery.

Acknowledgments

The authors gratefully acknowledge the support of the US Department of Energy Office of Electricity Storage Systems Program directed by Dr. Imre Gyuk and the University of Tennessee Governor's Chair Fund for support of this work.

Appendix I

List of Symbols

A	geometric area of the porous electrode
A_t	total internal surface area of the electrode
a	Nernstian diffusion layer thickness
b	thickness of the porous electrode
C_{dl}	area specific double layer capacitance
C_{fd2}	Area specific finite diffusion capacitance
D_O	Diffusion coefficient of oxidized species (V^{+3})
D_R	Diffusion coefficient of reduced species (V^{+2})
F	Faraday's constant
f	scale factor
i_o	exchange current density
i_s	Laplace transform of the current
p	pore size
P	Power factor for the constant phase element
R	gas constant
R_{ct}	charge transfer resistance
R_{fd1}	finite diffusion resistance
R_{hf}	ohmic resistance
s	Laplace transform variable $s = \sigma + j\omega$
T	absolute temperature
$[V^{+2}]_b$	concentration of V^{+2} in the bulk electrolyte
$[V^{+3}]_b$	concentration of V^{+3} in the bulk electrolyte
$[V^{+2}]_o$	surface concentration of V^{+2}
$[V^{+3}]_o$	surface concentration of V^{+3}
Z_a	complex impedance of a differential unit element of surface area within the electrode
Z'_a	complex impedance of the charge transfer reaction
Z'_{a1}	complex impedance of the charge transfer reaction limited by finite diffusion to a Nernstian layer (non-blocking boundary condition).
Z'_{a2}	complex impedance of the charge transfer reaction limited by finite diffusion within the pore walls (blocking boundary conditions)
Z_p	complex impedance of the porous electrode
α	anodic transfer coefficient
β	cathodic transfer coefficient
η	overvoltage
η_s	Laplace transforms of the overvoltage
σ	neperian frequency
ρ_1	specific ionic resistance within the electrode
ρ_2	specific electronic resistance of the electrode
ω	radian frequency

Appendix II

Parameters used to fit equations 1, 2, 3 and 28 to the data shown in Figure 1

A	5 cm^2	Direct measurement
A_t	150 cm^2	Calculated from total measured capacitance $A_t = C_T/C_{dl}$
a	1.45×10^{-2} cm	Fitting parameter
b	4×10^{-2} cm	Direct measurement
C_{dl}	2×10^{-5} F/cm^2	Typical double-layer capacitance
P	0.91	Direct measurement
D_O	7×10^{-6} cm^2/sec	Aqueous diffusion coefficient for V^{+3}
D_R	7×10^{-6} cm^2/sec	Aqueous diffusion coefficient for V^{+2}
f	0.068	Fitting parameter
i_o	1.08×10^{-5} A/cm^2	Obtained from Tafel plot (not shown)
T	303.15 K	Direct measurement
$[V^{+2}]_b$	1×10^{-5} mole/cm^3	Calculated using the Nernst equation and measured OCV
$[V^{+3}]_b$	7.9×10^{-4} mole/cm^3	Calculated using the Nernst equation and measured OCV
ρ_1	0.86 Ohm · cm	Electrolyte specific resistivity times the electrode porosity
ρ_2	0.012 Ohm · cm	Electrode specification, direct measurement

References

1. Z. Yang, J. Zhang, M. C. W. Kintner-Meyer, X. Lu, D. Choi, J. P. Lemmon, and J. Liu, *Chem. Rev.*, **111**, 3577 (2011).
2. J. E. Halls, A. Hawthornthwaite, R. J. Hepworth, N. A. Roberts, K. J. Wright, Y. Zhou, S. J. Haswell, S. K. Haywood, S. M. Kelly, N. S. Lawrence, and J. D. Wadhawan, *Energy Environ. Sci.*, **6**, 1026 (2013).
3. C. Ponce de León, A. Frías-Ferrer, J. González-García, D. A. Szánto, and F. C. Walsh, *J. Power Sources*, **160**, 716 (2006).
4. A. Z. Weber, M. M. Mench, J. P. Meyers, P. N. Ross, J. T. Gostick, and Q. Liu, *J. Appl. Electrochem.*, **41**, 1137 (2011).
5. E. Sum and M. Skyllas-Kazacos, *J. Power Sources*, **15**, 179 (1985).
6. M. Skyllas-Kazacos, *J. Electrochem Soc.*, **133**, 1057 (1986).
7. M. Rychcik and M. Skyllas-Kazacos, *J. Power Sources*, **19**, 45 (1987).
8. M. Rychcik and M. Skyllas-Kazacos, *J. Power Sources*, **22**, 59 (1988).
9. M. Kazacos, M. Cheng, and M. Skyllas-Kazacos, *J. Appl. Electrochem.*, **20**, 463 (1990).
10. W. Wang, Q. Luo, B. Li, X. Wei, L. Li, and Z. Yang, *Adv. Funct. Mater.*, **23**, 970 (2013).
11. J. Liu, J.-G. Zhang, Z. Yang, J. P. Lemmon, C. Imhoff, G. L. Graff, L. Li, J. Hu, C. Wang, J. Xiao, G. Xia, V. V. Viswanathan, S. Baskaran, V. Sprenkle, X. Li, Y. Shao, and B. Schwenzer, *Adv. Funct. Mater.*, **23**, 929 (2013).
12. D. Chen, M. A. Hickner, E. Agar, and E. C. Kumbur, *Electrochem. Commun.*, **26**, 37 (2013).
13. C. Ding, H. Zhang, X. Li, T. Liu, and F. Xing, *J. Phys. Chem. Lett.*, **4**, 1281 (2013).
14. H. Lee and H. Kim, *J. Appl. Electrochem.*, **43**, 553 (2013).
15. A. H. Whitehead and M. Harrer, *J. Power Sources*, **230**, 271 (2013).
16. W. Zhang, J. Xi, Z. Li, H. Zhou, L. Liu, Z. Wu, and X. Qiu, *Electrochim. Acta*, **89**, 429 (2013).
17. J. S. Lawton, D. S. Aaron, Z. Tang, and T. A. Zawodzinski, *J. Membr. Sci.*, **428**, 38 (2013).
18. M. Zhang, M. Moore, J. S. Watson, T. A. Zawodzinski, and R. M. Counce, *J. Electrochem Soc.*, **159**, A1183 (2012).
19. M. Kazacos and M. Skyllas-Kazacos, US Patent 6,468,688 B2
20. L. Li, S. Kim, W. Wang, M. Vijayakumar, Z. Nie, B. Chen, J. Zhang, G. Xia, J. Hu, G. Graff, J. Liu, and Z. Yang, *Adv. Eng. Mater.*, **1**, 394 (2011).
21. D. S. Aaron, Q. Liu, Z. Tang, G. M. Grim, A. B. Papandrew, A. Turhan, T. A. Zawodzinski, and M. M. Mench, *J. Power Sources*, **206**, 450 (2012).
22. Q. H. Liu, G. M. Grim, A. B. Papandrew, A. Turhan, T. A. Zawodzinski, and M. M. Mench, *J. Electrochem Soc.*, **159**, A1246 (2012).
23. C.-N. Sun, F. M. Delnick, D. S. Aaron, A. B. Papandrew, M. M. Mench, and T. A. Zawodzinski, *ECS Electrochem. Lett.*, **2**, A43 (2013).
24. D. S. Aaron, Z. Tang, J. S. Lawton, A. P. Papandrew, and T. A. Zawodzinski Jr., *ECS Trans.*, **41**(23), 43 (2012).
25. D. Aaron, C.-N. Sun, M. Bright, A. B. Papandrew, M. M. Mench, and T. A. Zawodzinski, *ECS Electrochem. Lett.*, **2**, A29 (2013).
26. R. Darling and M. Perry, *ECS Trans.*, **53**, 31 (2013).
27. C.-N Sun, F. M. Delnick, L. Baggetto, G. M. Veith, and T. A. Zawodzinski, *J. Power Sources*, **248**, 560 (2014).
28. G. Paasch, K. Micka, and P. Gersdorf, *Electrochim. Acta*, **38**, 2653 (1993).
29. T. Jacobsen and K. West, *Electrochim. Acta*, **40**, 255 (1995).
30. F. M. Delnick, S. Motupally, and Y. Zhang, in *The 14th International Seminar on Double layer Capacitors and Hybrid Energy Storage Devices*, 2004, 5-17.
31. E. Agar, C. R. Dennison, K. W. Knehr, and E. C. Kumbur, *J. Power Sources*, **225**, 89 (2013).